Measurement of Internal Temperatures in Engine-Scale Gas Turbine Blade with Fiber Optic Sensors

Emily K. Berexa*, Ben Coulton[†], Julian A.J. Fells[‡], and Peter T. Ireland[§]
Dept. of Engineering Science, University of Oxford, Oxford, OX1 3PJ, United Kingdom

Further improvements in performance of gas turbine engines require increases in turbine entry temperature. As these temperatures continue to exceed the material properties of turbine blades, complex cooling configurations, advanced manufacturing techniques, and thermal barrier coatings are required to protect blades from damage. While external surface temperatures can be measured to evaluate the effectiveness of such systems, limited techniques exist to capture internal metal temperatures due to the small size of engine-scale blades and the complex cooling configurations they contain. However, knowledge of these temperatures is essential to optimizing and managing thermal gradients within the blade and ensuring blade life. The capability to measure internal metal temperatures would enable more comprehensive analyses of blade performance and life, contributing invaluable data to the research and development process. This paper explores the use of fiber optic sensors to measure temperature fields with high spatial resolution in difficult-to-access blade locations. Changes in temperature can be monitored through changes in the reflected wavelength of fiber Bragg gratings, or narrow band filters inscribed in the core of an optical fiber. The gratings are resistant to the harsh conditions and high temperatures present in gas turbines. Many gratings can be written along a single waveguide with a diameter of 0.15 mm, resulting in a minimally invasive instrumentation technique. In this investigation, a cooled, engine-scale turbine blade is instrumented with fiber optic sensors and exposed to high temperatures in the Oxford High Temperature Linear Cascade at the Oxford Thermofluids Institute.

I. Nomenclature

Λ_G = Period of refractive index modulation of grating, *nm*
α = Thermal expansion coefficient, $°C^{-1}$
η_{eff} = Effective refractive index in the fibre
λ_B = Bragg Wavelength, *nm*
ϕ = Cooling effectiveness
ζ = Thermo-optic coefficient, $°C^{-1}$
T_{c_in} = Coolant inlet temperature, $°C$
T_g = Mainstream gas temperature, $°C$
T_m = Blade metal temperature, $°C$

II. Introduction and Motivation

Further advances in gas turbine engine performance require increases in the turbine entry temperature, or the temperature exiting the combustor and entering the turbine. Elevated turbine entry temperatures (TET) drive improvements in power output and engine efficiency. However, optimization of cooling systems, thermal barrier coatings, and advanced manufacturing techniques is necessary to protect the turbine blade from TETs exceeding the material properties of the metal.

As the blade is exposed to mainstream temperatures of at least 1700°C [1], coolant is routed through internal passages, reducing the mean metal temperature and producing thermal gradients within the blade. Given the impact of such

---

*DPhil Candidate, Dept. of Engineering Science, University of Oxford. U.S. Air Force. Corresponding author: emily.berexa@eng.ox.ac.uk.
[†] DPhil Candidate, Dept. of Engineering Science, University of Oxford.
[‡] EPSRC Research Fellow, Dept. of Engineering Science, University of Oxford.
[§] Director, Oxford Thermofluids Institute, Dept. of Engineering Science, University of Oxford.

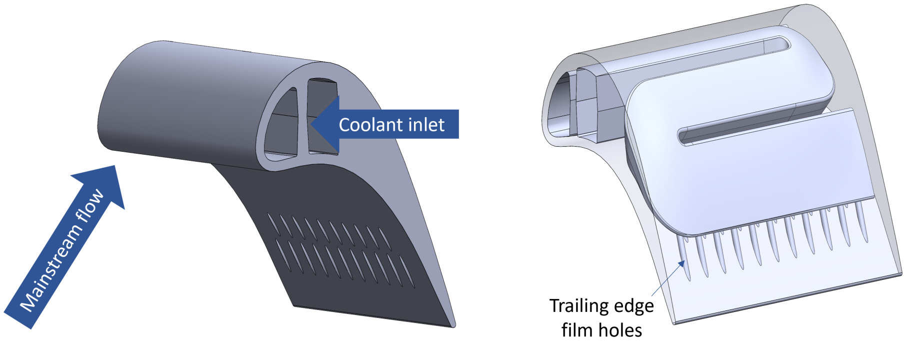

Fig. 1 Design of geometry tested in Oxford High Temperature Linear Cascade.

gradients on thermal stresses and strains, managing the thermal field is crucial to protecting the blade and ensuring blade life. Knowledge of the temperatures within the blade can also provide insight into the performance of the cooling system and highlight potential hotspots. The conventional method of predicting blade temperatures combines a finite element thermal analysis with heat transfer coefficients from empirical correlations or CFD, correlations for film effectiveness, and a flow network. While established experimental methods exist to capture the surface metal temperatures, limited techniques exist to measure internal metal temperatures, despite their centrality to blade performance and lifing. Due to the small scales and intricate cooling configurations of turbine blades, it is difficult to instrument internal surfaces without impacting blade performance. As a result, experimental work is often conducted on scaled up geometries, or computational methods are employed to model and interpolate the internal temperatures, using experimentally-captured external temperatures as boundary conditions. An improved ability to measure internal temperatures could provide critical experimental data to the design process and support validation of computational models.

This study investigated the application of fiber optic sensors to measure blade internal metal temperatures with high accuracy and spatial resolution. With the capability to measure temperature at numerous points along fibers with diameters of 0.15 mm, fiber Bragg gratings (FBGs) were explored as a minimally invasive method of instrumenting turbine blades.

III. Investigation Overview

This work embedded fiber optic sensors within a gas turbine blade representative of state of the art cooling technology. Evaluation of sensor performance was conducted in the Oxford High Temperature Linear Cascade (HTLC), a novel facility at the Oxford Thermofluids Institute designed to test engine-scale, cooled turbine blades [2]. The internal metal temperature measurements acquired with fiber optic sensors were validated with a thermocouple embedded within the blade.

Design of an engine-scale blade with a serpentine multi-pass cooling configuration was conducted. The blade was designed to be representative of current industry technology, containing serpentine cooling passages and film cooling, as shown in Fig. 1. The small size of an engine-scale turbine blade and the high spatial resolution necessary for meaningful measurements were identified as the primary challenges associated with installation of fiber optic sensors. It was determined that engine-representative passage sizes and wall thicknesses were necessary to evaluate the viability of embedding fiber optic sensors. To address these challenges while minimizing unnecessary complexity in the modelling and manufacturing of the blade, additional internal cooling features such as impingement cooling, passage ribs and turbulators were not included in the design.

A preliminary network analysis was undertaken to size the cooling passages and film cooling holes of the blade. The performance of the blade was then evaluated and the geometry modified based on the results of a conjugate heat transfer analysis in ANSYS Fluent. The sensor configuration was optimized to measure the anticipated thermal gradients while minimizing disturbance to the thermal field.

Metal temperature measurements were acquired in the web between the first two channels of the serpentine cooling passage. The blade was spliced in this region and additively manufactured in two sections, allowing for shallow grooves

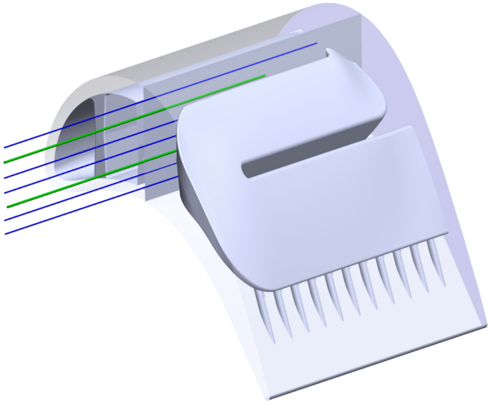

Fig. 2 Engine-scale blade instrumented with 5 optical fibers (blue) each containing 5 temperature sensors and 2 thermocouples (green) to be tested in Oxford High Temperature Linear Cascade.

to be spark eroded and the fibers and thermocouples installed in the web of interest, as shown in Fig. 2.

Upon completion of instrumentation, the fiber optic sensors and thermocouples underwent a validation process in a high temperature laboratory oven. The test piece was exposed to known temperature conditions similar to those expected in the HTLC, establishing confidence in the fiber optic sensor system and installation process. The blade was then installed in the HTLC, and coolant and hot mainstream flow were introduced. The resulting temperatures through the web were measured with fiber optic sensors and validated with thermocouple measurements.

IV. Technical Foundation

A. Fiber Optic Sensors

Optical fibers transmit information in the form of light and are commonly used in telecommunications and data transfer applications due to their low transmission losses, high bandwidth capacity, and immunity to electromagnetic interference. Given their small diameter and resistance to extreme conditions, optical fibers have also been used in sensing applications in diverse fields, from the oil and gas industry to the biomedical sector [3],[4]. Various sensing techniques exist, such as Fabry-Perot sensors, Raman scattering, Rayleigh scattering, and fiber Bragg gratings [5].

Fiber Bragg gratings (FBGs) are of particular interest in this application due to their status as a well-established, quasi-distributed sensing technique with high signal-to-noise ratio, good sensitivity, high spatial resolution, and resistance to harsh conditions. High spatial resolution can be achieved through multiplexing, or the placement of many sensors along a single fiber.

Each sensor is comprised of a grating in the core of the silica waveguide, which causes a periodic modulation of the effective refractive index of the core. The modulation results in a narrow band filter which reflects a specific range of wavelengths. The reflected, or Bragg, wavelength is impacted by physical parameters such as temperature and strain, which allow the FBGs to provide information about the fibers' surrounding. The interrogator provides a signal via a light source such a superluminescent diode (SLED) or tunable laser and then classifies the reflected wavelength using photodiodes. With wavelength division multiplexing, many sensors with different Bragg wavelengths can be placed along a single fiber and read by an interrogator, generating minimally-invasive measurements with high spatial resolution.

The Bragg wavelength (λ_B) is dependent on the effective refractive index of the fiber and the period of the modulation of the grating, as shown in Eq. (1). Changes in temperature impact both parameters, as captured by the thermo-optic coefficient (ζ) and the thermal expansion coefficient (α) in Eqs. (2) and (3), respectively. The impact of changing temperature on Bragg wavelength is evident in Eq. (4).

$$\lambda_B = 2\eta_{eff}\Lambda_G \tag{1}$$

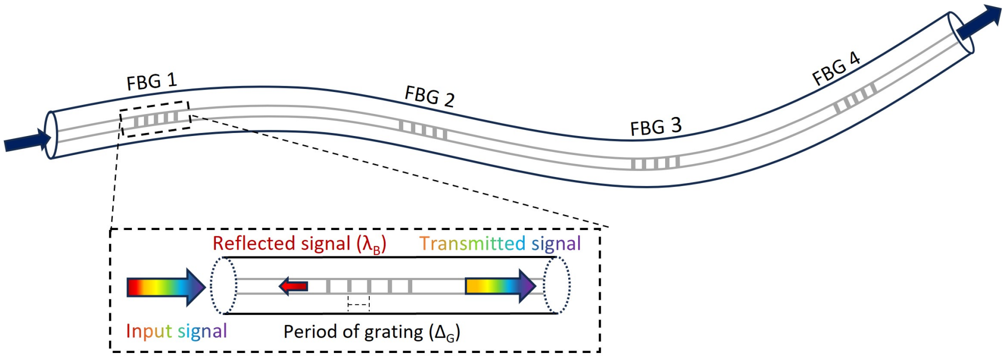

Fig. 3 Schematic of FBGs inscribed in fibre optic waveguide. Adapted from [3].

$$\zeta = \frac{1}{\eta_{eff}} \frac{\delta \eta_{eff}}{\delta T} \tag{2}$$

$$\alpha = \frac{1}{\Lambda_G} \frac{\delta \Lambda_G}{\delta T} \tag{3}$$

$$\Delta \lambda_B = \lambda_B (\alpha + \zeta) \Delta T \tag{4}$$

From Eq. (4), a theoretical temperature sensitivity of approximately 14 pm/°C can be calculated for a silica-based waveguide ($\zeta = 8.6 \times 10^{-6}\ ^\circ\mathrm{C}^{-1}$, $\alpha = 0.55 \times 10^{-6}\ ^\circ\mathrm{C}^{-1}$) [6]. However, this value varies in application due to losses in the fiber, the variation of α with temperature, and differences in fiber coating and the composition of the core.

Strain on the fiber impacts the Bragg wavelength in a similar manner to temperature, altering the refractive index and period of the grating. As a result, it can be difficult to distinguish between the effects of strain and temperature on the FBG. The fiber must be installed in such a way to isolate the impacts of one parameter, or a method of decoupling the two parameters must be employed. Various techniques of reducing the cross-sensitivity and discerning between the impacts of strain and temperature have been explored, including dual-wavelength FBGs [7], FBGs inscribed in fibers of different diameters [8], and the use of high birefringence bow-tie fiber [9].

B. Applications of Fiber Optic Sensors to Turbomachinery

While limited research has been conducted regarding the use of fiber optic sensors to measure internal metal temperatures in gas turbines, other applications to turbomachinery have been explored. The authors in [10] embedded fiber optic sensors in the exhaust path of a power station gas turbine and in a heat shield tile on the side of a combustion rig. They cycled various sensors up to high temperatures over multiple months and found that femtosecond-inscribed silica FBGs (fs-FBGs) performed well, maintaining sufficient accuracy above 800°C. Sapphire FBGs also performed very well, remaining stable at temperatures up to 1200°C. However, sapphire FBGs present additional challenges due to their multimode nature; authors such as [11] are working to address this issue through the development of single mode sapphire FBGs. The higher temperature capabilities of sapphire FBGs would create valuable opportunities for monitoring at engine-representative conditions in turbomachinery.

The authors in [12] and [13] conducted similar studies evaluating the ability of FBGs to endure the harsh conditions present in turbomachinery. In [12], ultraviolet-written FBGs were packaged in a circumferential cable and radial rake to measure gas turbine exhaust temperatures. The sensors were subjected to temperatures up to 650°C and performed well in terms of spatial resolution and dynamic response. In [13], fs-FBGs were packaged in stainless steel tubing and successfully used to measure combustor sidewall and exhaust gas gradients at temperatures above 1000°C.

More recently, the authors in [14] embedded FBGs in metal test specimens and exposed them to thermal cycling to evaluate their applications in component health monitoring for rotorcraft. While the FBGs experienced some degradation in long duration testing at around 700°C, they survived at shorter durations and lower temperatures. Confidence was established for the application of FBGs to gas turbine monitoring, and the authors call for further sensor maturation and development of design and manufacturing methods.

An initial investigation was undertaken by the authors into the impacts of embedding sensors within engine-scale test pieces in [15]. Fibers were installed in tight bend radii representative of possible routing configurations in turbine blades (3.5, 5, 7.5, 10 mm). The authors found that excessive transmission losses were unlikely to occur in these configurations. However, decreases in reflected wavelength were observed near the apex of small bend radii, suggesting that caution should be taken when installing sensors directly in the bend.

The impact of increasing temperature on the fibers was also explored. The sensors were first calibrated to determine the relationship between temperature and wavelength. The fibers were then installed in metal test pieces and exposed to varying thermal profiles. The authors found that bonding the fiber at one or two points resulted in more accurate temperature measurements, perhaps due to improved thermal contact. This finding guided the decision to bond the fiber at entry to the test piece in the current investigation. The fibers were then installed in a metal test piece with tight bend radii and the impact of increasing temperature observed. The authors again found that bonding the fiber is beneficial for accuracy and that sensor placement near the apex can impact reflected wavelength. The authors suggested that sensors should be placed at sufficient distance from the apex of the curve or re-calibrated following installation in the test piece. This study aims to minimize the exposure of fibers to bending.

V. Blade Design and Experimental Procedures

A. Test Piece Manufacture and Sensor Installation

To evaluate the viability of capturing internal metal temperatures with FBGs, fibers were installed in an engine-scale turbine blade with representative cooling technology. With a chord length of approximately 34 mm, the blade contained a leading edge passage and a rear-flowing, triple-pass passage. The trailing edge channel of the triple pass contained two rows of film cooling holes (diameter (D) = 0.85 mm, pitch = 4.2*D). A preliminary network analysis was conducted to size the channels and film holes to achieve reasonable passage Mach numbers, Reynolds numbers, Nusselt numbers, and heat transfer coefficients. The geometry is displayed in Fig. 1.

The blade was additively manufactured in Stainless Steel 316 using direct metal printing (DMP). As displayed in 4, the blade was split along the plane of sensor installation and printed in two sections. The sensor grooves were then machined using electrical discharge machining (EDM). With a web thickness ranging from 1.25 to 2.0 mm, care was taken to minimize the depth of the cavities and the disruption to the geometry. Five grooves of depth 0.22 mm were spark eroded for the fibers, and two grooves of depth 0.3 mm were spark eroded for the thermocouples. Subsequent work has shown that it should be possible to machine the holes directly into the aerofoil without including a split.

The two sections of the blade were bonded using a high temperature epoxy resin, and two Type K thermocouples of diameter 0.25 mm were installed in the larger grooves. One thermocouple deviated from its position adjacent to the FBGs prior to testing and so is not discussed in Section VI. Five fibers containing five FBGs each were then installed in the blade. Each fiber was coated in thermal grease and placed unbonded in the cavity to minimize the differential thermal expansion of the metal test piece and the silica fiber. This aimed to reduce any potential temperature and strain cross-sensitivity, as discussed in Section IV. To secure the fibers and reduce positional uncertainty, each fiber was bonded at entry to the blade with high temperature silicone. Twenty-five point measurements can be captured with the FBGs in the region of interest, as shown in Fig. 5. The instrumented blade is show in Fig. 6.

B. Experimental Procedures

Prior to installation in the test piece, calibration of the fiber optic sensors was conducted in a high temperature laboratory oven. The reflected wavelength for each sensor was recorded and compared to temperature measurements acquired with Type K thermocouples. Following instrumentation, the sensor installation and calibration were validated by again comparing FBG and thermocouple readings acquired in the high temperature oven.

Primary testing occurred in the Oxford High Temperature Linear Cascade (HTLC), a novel facility designed to test engine-scale, cooled turbine blades [2]. A schematic of the HTLC test section is included in Fig. 1. The blade was subjected to mainstream flow at a Reynolds number and temperature of approximately 770,000, and 205°C, respectively. Coolant was introduced into the blade at ambient temperature (approximately 22°C), and testing occurred at coolant-to-mainstream pressure ratios of 0.95, 1.14, 1.36, 1.51, and 1.65. Temperature measurements were acquired by the thermocouple and a calibrated data logger at a frequency of 3.3 Hz. Wavelength measurements were acquired by the interrogator and fiber Bragg gratings at a frequency of 10 Hz.

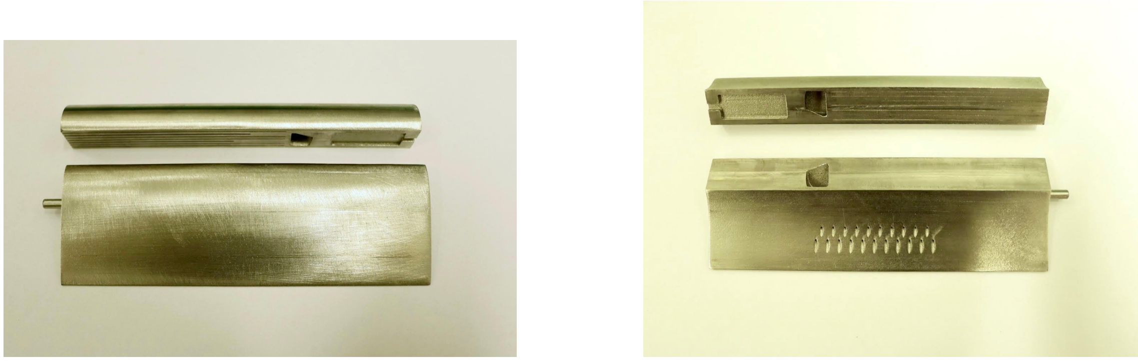

(a) View of suction surface of blade. **(b) View of pressure surface of blade.**

(c) EDM fiber and thermocouple cavities. **(d) Entry point of sensors into blade.**

Fig. 4 Additively manufactured test piece with EDM cavities for fiber optic sensors and thermocouples.

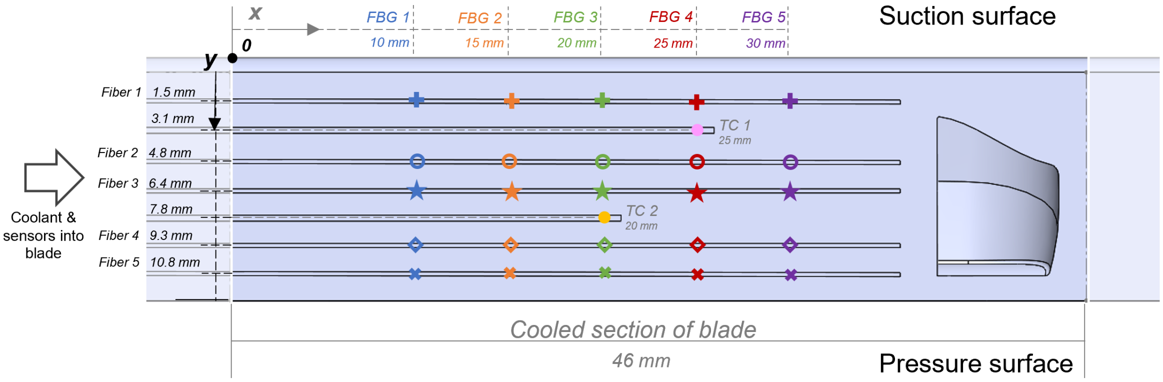

Fig. 5 Cross-sectional view of plane of sensor installation containing FBGs and thermocouples.

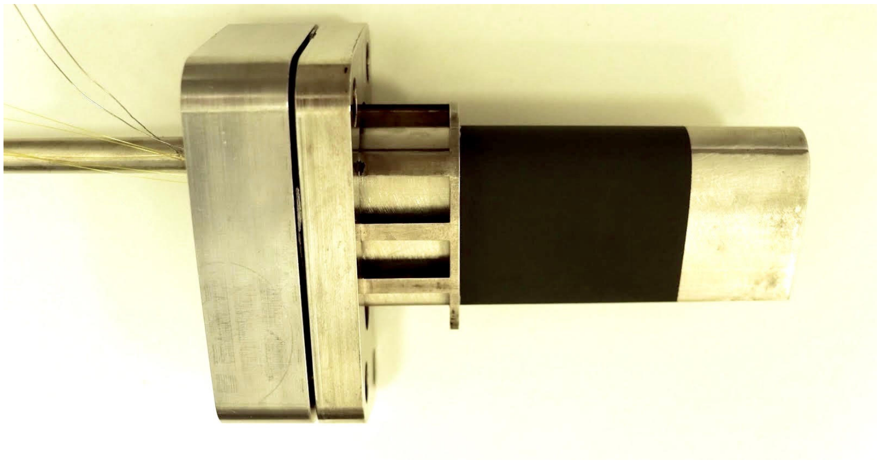

Fig. 6 Instrumented blade with five fibers and two Type K thermocouples installed.

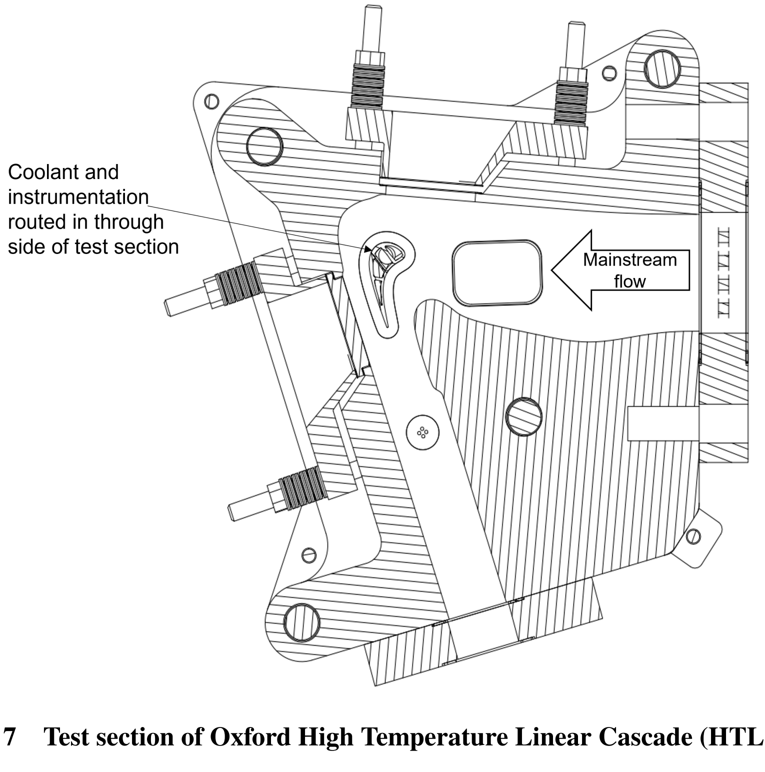

Fig. 7 Test section of Oxford High Temperature Linear Cascade (HTLC) [2].

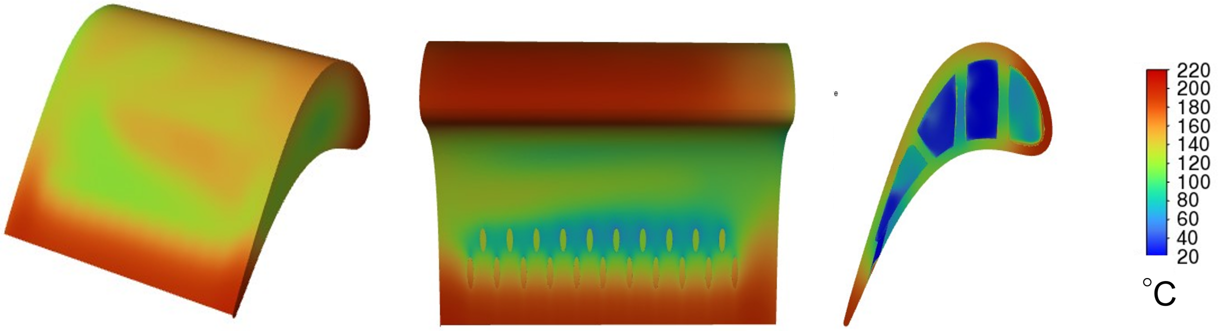

Fig. 8 Conjugate heat transfer analysis for pressure ratio = 1.36.

C. Conjugate Heat Transfer Analysis

Prior to experimental testing, a conjugate heat transfer analysis was conducted in ANSYS Fluent. A steady state simulation modelled the convective heat transfer between the blade and coolant and the conductive heat transfer within the blade. The $k - \omega$ Shear Stress Transport (SST) turbulence model was used. The coolant inlet was assigned as a pressure inlet, while the film cooling holes were assigned as pressure outlets based on a scaled engine pressure distribution. Simulations were conducted at the gas temperatures and coolant-to-mainstream pressure ratios expected during testing.

The effects of the mainstream flow and film cooling holes were mapped onto the surface of the blade using the method developed by the authors in [16]. A convective heat transfer boundary condition was applied to the external surface with varying heat transfer coefficients and external temperatures. The heat transfer coefficient distribution over the surface of the blade was calculated using Ambrok's approach for a turbulent boundary layer with varying freestream velocity, as detailed in [17]. The leading edge of the blade was treated as a two-dimensional cylinder, as applied by [18].

To model the effects of the film cooling holes on the external surface, a modified form of the Goldstein equation was used as proposed by [19] and modified by [16]. Blowing ratio and mass averaged temperature were calculated with each iteration, and the latter was specified as the effective external film temperature driving the heat transfer. The effects of the film holes were combined using the Sellers superposition method and mapped onto the surface using a user-defined function (UDF) as the simulation progressed [20].

An overview of the conjugate heat transfer analysis results at a coolant-to-mainstream pressure ratio of 1.36 is displayed in Fig. 8. Comparison to experimental data collected in the HTLC is included in Section VI.

VI. Results and Discussion

A. Sensor Calibration

Prior to installation in the test piece, the sensors were exposed to varying thermal profiles and calibrated in a high temperature oven. Wavelength readings were acquired from all 25 sensors, and temperature measurements were captured with Type K thermocouples. Five runs were conducted from 25 to 300°C. The temperature sensitivity of each FBG was determined to be around 13 pm/°C. For example, the relationship between temperature and wavelength can be characterized as $\lambda = 0.01306 * T + 1540.64$ for Fiber 5 FBG 2 (sensitivity of 13.06 pm/°C). With the approach outlined in [21], it was determined that there is a 95% probability that the true value for the temperature sensitivity lies within the range 13.06±1.24 pm/°C. This value represents 9.6% of the temperature sensitivity of the FBG. The sensitivity is within the range of the theoretical value discussed in Section IV.A, which varies with the physical composition of the core and cladding, losses in the fiber, and the variation of the coefficient of thermal expansion of the silica with temperature.

To account for the variation of the coefficient of thermal expansion over the full temperature range, a polynomial regression was performed for each sensor to more accurately model the data. An example of a fifth-order polynomial regression for a single FBG is included in Fig. 9. Correlation coefficients for all regressions were greater than (0.999).

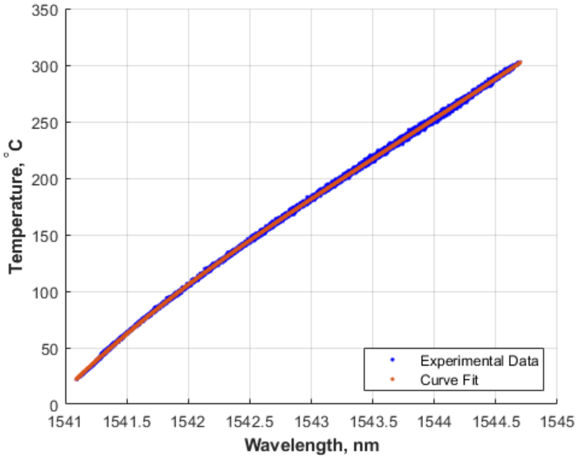

Fig. 9 Polynomial regression capturing relationship between wavelength and temperature for Fiber 5 FBG 2.

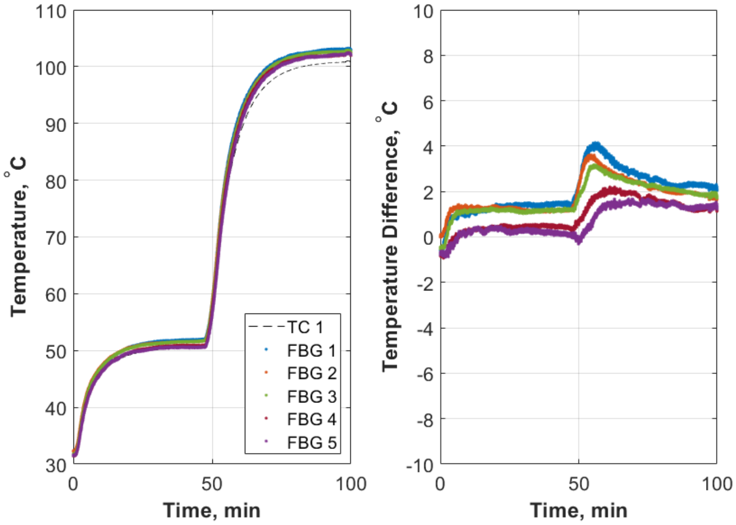

Fig. 10 Temperature as measured by embedded thermocouple and FBGs during test piece validation in high temperature oven (Fiber 2).

With confidence established in the wavelength response to temperature, the fibers were installed in the test piece.

B. Test Piece Validation

Following instrumentation of the test piece, the temperature sensitivities determined during calibration were validated in a high temperature oven. The test piece was exposed to varying profiles with temperatures comparable to those expected during testing. The calibration coefficients were applied to wavelength readings and the temperatures measured by the thermocouple and FBGs were compared. An accuracy of ±2.2°C can be assumed for the Type K thermocouple [22]. Considering the temperature sensitivity of the grating and the wavelength accuracy and sensitivity of the interrogator, an uncertainty of ±0.8 °C was expected for the temperature measurement derived from reflected wavelength.

An example of a validation run is included in Fig. 10. Slight variations between the thermocouples and FBGs were expected during transient conditions due to varying locations of sensors within the blade. When the calibration values were applied, four of the five fibers showed agreement with the thermocouple temperatures, with an average difference of 2.2°C across the 6 runs. However, greater differences were observed in Fiber 1.

A summary of the temperature sensitivity for each FBG before and after installation is shown in Fig. 11. As is

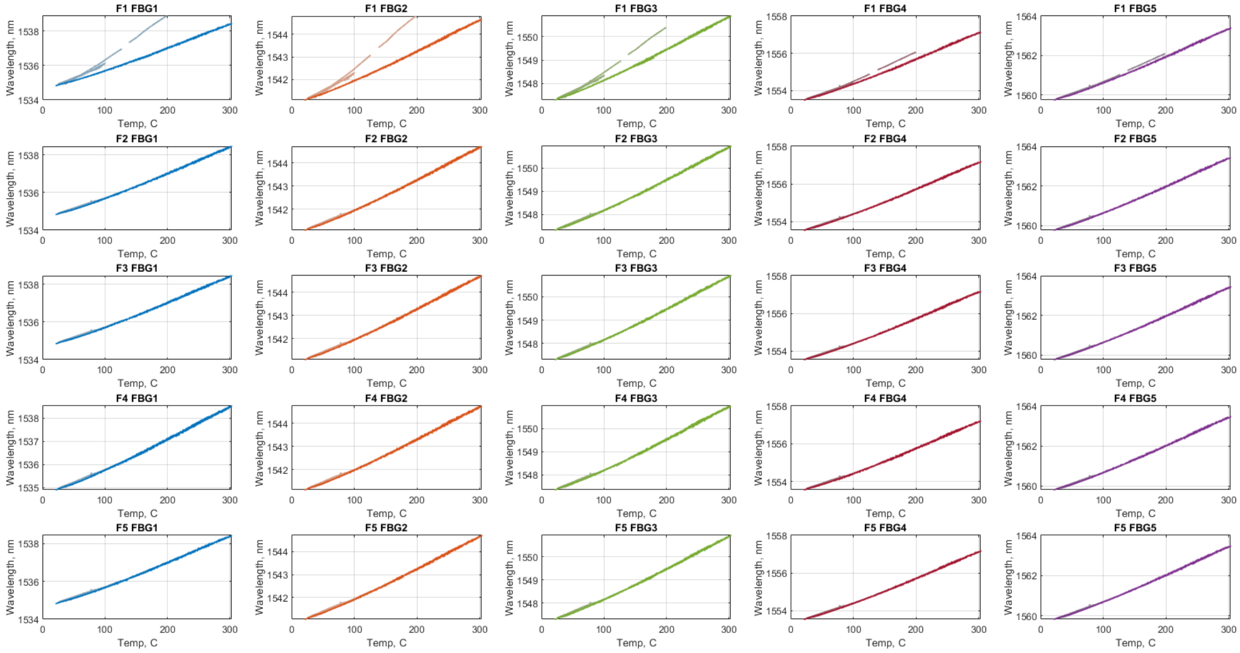

Fig. 11 Temperature sensitivity of FBGs before and after installation in test piece.

evident by the presence of a single linear relationship, Fibers 2-5 displayed the same temperature sensitivity during calibration and after installation. However, Fiber 1 exhibited different behavior during validation (indicated in the lighter shade) than that observed during calibration (indicated in the darker shade). A possible bonding between the test piece and the fiber during installation could cause this increase in temperature sensitivity. If mechanically coupled with the test piece, the differential coefficient of thermal expansion between the stainless steel test piece and the silica fiber could cause additional strain on the fiber, resulting in a higher wavelength reading at a given temperature.

To evaluate the feasibility of in-situ calibration in such circumstances, the fiber was re-calibrated based on the temperature and wavelength readings from the validation run. It should be noted that the positional differences of the fiber and the thermocouple introduce uncertainty into the calibration. Additionally, the calibration was conducted over a lower temperature range and a reduced number of runs to prevent extensive thermal cycling of the test piece and epoxy prior to testing. This prompted the use of a linear regression as opposed to a polynomial regression for Fiber 1. The success of the re-calibration was evaluated during testing in the HTLC.

C. Testing in High Temperature Linear Cascade

Following calibration and validation, testing commenced in the HTLC. Internal metal temperatures were captured at 26 different points with the FBGs and the thermocouple. The coolant mass flow was varied throughout testing in order to establish the following pressure ratios: 0.95, 1.14, 1.36, 1.51, and 1.65. For each pressure ratio, the mean metal temperature at each sensor location was recorded, as shown in Fig. 12. The symbols on the plots in Fig. 12a and 12b correlate to the symbols displayed in Fig. 5. For example, FBG 1 on Fiber 1, which is displayed as a blue cross in Fig. 5, is positioned in the upper left corner of both plots. Fiber 1 is positioned nearest the suction surface of the blade, while Fiber 5 is positioned nearest the pressure surface. The filled-in circle represents the thermocouple embedded within the blade.

As demonstrated in Fig. 12, the temperature measurements captured by the FBGs and thermocouple capture the thermal gradients within the region of interest. Given its position within the blade, the thermocouple is expected to reflect a temperature similar to those acquired by FBG 4 on Fibers 1 and 2. At a pressure ratio of 0.95, Fiber 1 FBG 4 and Fiber 2 FBG 4 recorded temperatures of 141.6°C and 145.0°C, respectively. The thermocouple measured a temperature of 154.5°C. Similarly, at a pressure ratio of 1.36, Fiber 1 FBG 4 and Fiber 2 FBG 4 recorded temperatures of 51.1°C and 36.9°C, respectively. The thermocouple measured a temperature directly between these two, recording a value of 45.5°C. For all pressure ratios, the thermocouple remained within 15°C and 9°C of the temperatures recorded

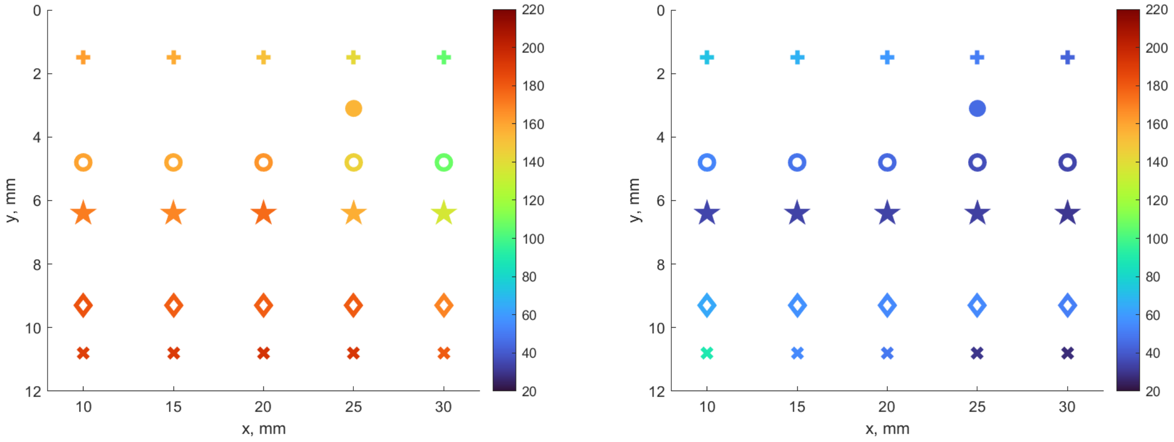

(a) Metal temperature (°C) at pressure ratio = 0.95.

(b) Metal temperature (°C) at pressure ratio = 1.36.

Fig. 12 Metal temperature (°C) captured by each FBG and thermocouple at locations shown in Fig. 5.

by Fiber 1 FBG 4 and Fiber 2 FBG 5, respectively. Given the high thermal gradients expected within the blade, this concurrence establishes confidence in the temperature measurements acquired with the FBGs.It should be noted that a higher degree of uncertainty is expected for Fiber 1 given the reduced number of runs and calibration range.

Given the small diameter of the fiber and the ability to inscribe many FBGs along a single fiber, a high density of senors was able to be installed within the approximately 1.5 mm-wide web. Temperature measurements were captured every 5 mm in the x-direction, and every 1.5-1.6 mm in the y-direction. The high spatial resolution allowed for a detailed understanding of the thermal gradients within the metal web of the blade, which are displayed in solid lines for a pressure ratio of 1.36 in Fig. 13.

The symbols contained in the plots again correlate to the symbols shown in Fig. 5. Each marker type (cross, diamond, etc.) corresponds to a fiber, while each color corresponds to a specific FBG along each fiber. Fig. 13a captures the change in temperature along the y-axis as shown in Fig. 5. Low values of y correspond to Fibers 1 and 2, which are closer to the suction surface. High values of y represent Fibers 4 and 5, which are closer to the pressure surface. Therefore, Fig. 13a captures a decrease in temperature from the suction surface to Fiber 3, at the mid-point of the web. An increase is observed from the mid-point to Fiber 4. Significant spread is then observed across Fiber 5, which might be attributed to a leak caused by the failure of the glue at higher pressure ratios. FBGs 4 and 5, nearest the coolant passage, recorded a value similar to the coolant temperature. As the test piece experienced thermal cycling causing the glue to expand and contract, damage was likely done to Fiber 5 as the wavelength reflection was lost from FBGs 4 and 5. This suggests that care must taken to ensure the fibers remain in the cavities and are not subjected to damage due to the thermal expansion of the test piece. However, the thermal gradients captured by Fibers 1-4 and the concurrence of the thermocouple suggest that temperatures can be successfully captured with fiber optic sensors.

Fig. 13b captures the thermal gradients in the x-direction, or from left to right in 5. The blue markers represent FBG 1 on each fiber, while the purple markers represent FBG 5 on each fiber. A decrease in temperature was generally observed from FBG 1 to FBG 5, which was positioned nearest the cooling passage.

To further characterize the performance of the cooling system, the cooling effectiveness (ϕ) at each sensor location within the blade was calculated based on the measured blade metal temperatures (T_m), the mainstream gas temperature (T_g), and the coolant inlet temperature ($T_{c,in}$):

$$\phi = \frac{T_g - T_m}{T_g - T_{c,in}} \tag{5}$$

The cooling effectiveness values for pressure ratios 0.95 and 1.36 are displayed in Fig. 14. The FBGs and thermocouple all captured an increase in cooling effectiveness as the coolant mass flow increased.

The cooling effectiveness measured by the FBGs could then be compared to the thermal field modelled in Section V.C. Fig. 15 superimposes the cooling effectiveness values measured during testing on the results of the conjugate heat transfer analysis. At pressure ratios above 0.95, higher cooling effectiveness values were measured than predicted, and

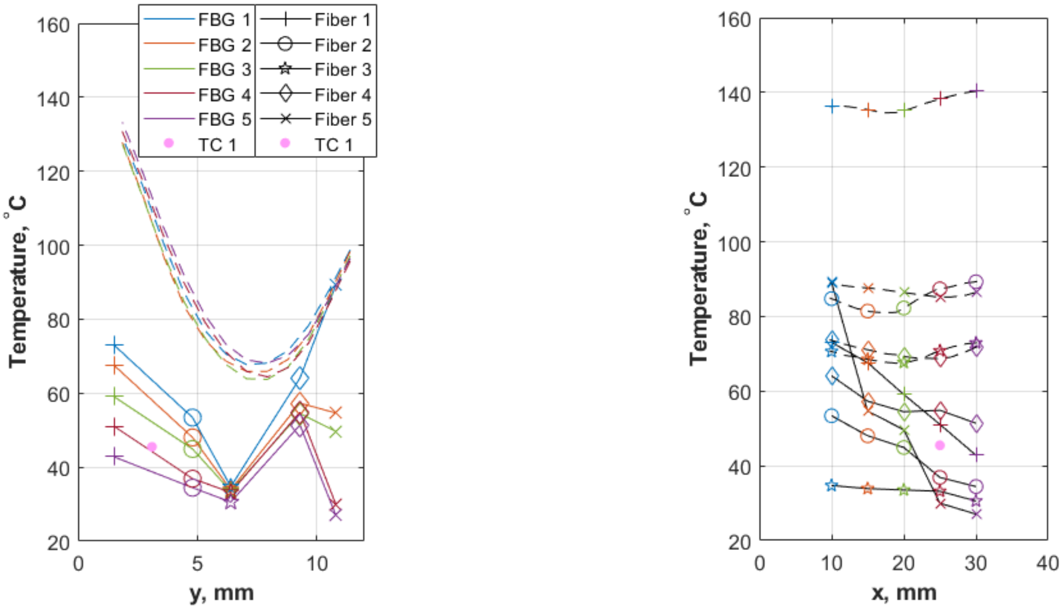

(a) Temperature from the suction surface (y = 0 mm) to the pressure surface (y = 12mm) of the blade.

(b) Temperature in the spanwise direction

Fig. 13 Metal temperature (°C) as predicted by conjugate heat transfer analysis (dashed lines) and as measured by each FBG and thermocouple (solid lines) at pressure ratio = 1.36.

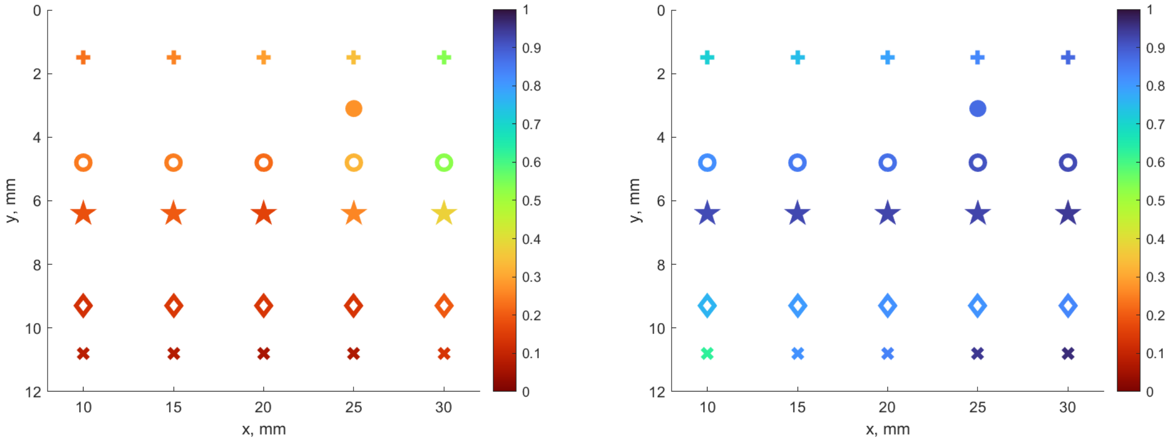

(a) Cooling effectiveness at pressure ratio = 0.95.

(b) Cooling effectiveness at pressure ratio = 1.36.

Fig. 14 Cooling effectiveness captured by each FBG and thermocouple (a, b) at locations shown in (5).

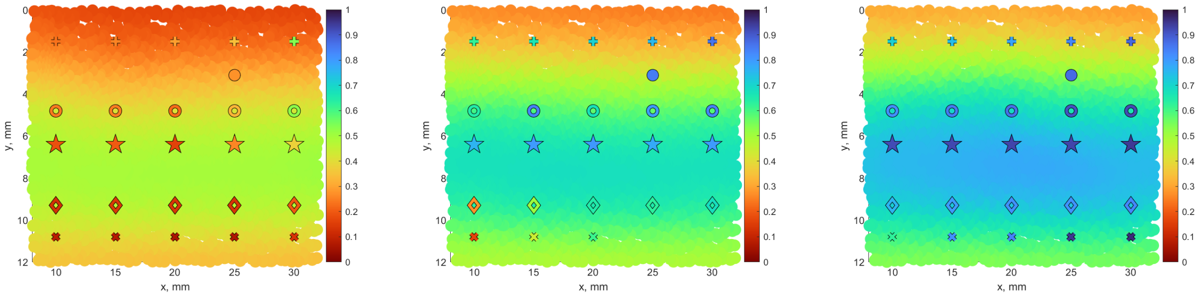

(a) Pressure ratio = 0.95. **(b) Pressure ratio = 1.14.** **(c) Pressure ratio = 1.36.**

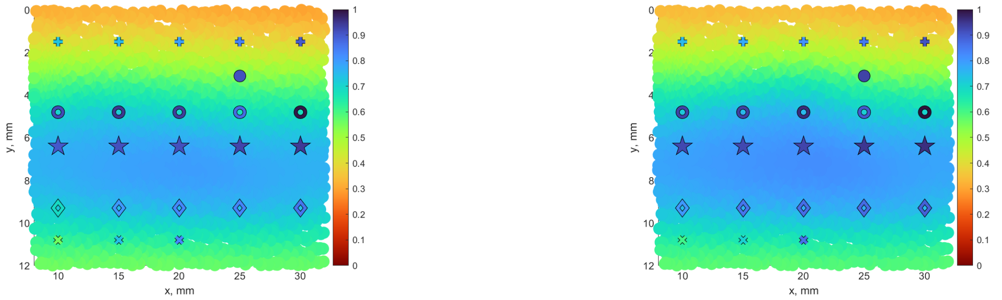

(d) Pressure ratio = 1.51. **(e) Pressure ratio = 1.65.**

Fig. 15 Cooling effectiveness as measured by fiber Bragg gratings and thermocouple superimposed on results of conjugate heat transfer analysis.

Fiber 1 displayed the greatest difference from the computational model. Possible causes for the differences are being investigated and the computational model further developed. However, general trends could be observed in both the experimental data and the CFD. For example, a decrease in temperature was observed in the fiber furthest from the mainstream flow (Fiber 3), as is evident in Fig. 13, where the simulation data is displayed by the dashed lines.

VII. Conclusion and Research Outlook

Given the ability to inscribe multiple FBGs along a fiber of diameter 0.15 mm, fiber optic sensors show promise as a minimally invasive instrumentation technique. This work embedded fiber Bragg gratings within the web of an engine-scale turbine blade to measure metal temperatures with high spatial resolution. A detailed understanding of the thermal field within the web was developed with 25 fiber optic temperature sensors and a thermocouple for validation. Confidence was established in the ability of FBGs to measure internal metal temperatures with high spatial resolution.

Additional geometries are being designed to further explore the applications of fiber optics to measuring metal temperatures and cooling effectiveness. The following work is being undertaken: 1) further validation of FBG measurements with additional embedded thermocouples, 2) exploration into methods of spark eroding sensor cavities directly into a blade, minimizing the need to manufacture in two pieces, 3) investigation into fiber performance, including the interaction between the fibers and the metal test piece and the accuracy of FBGs in high temperature gradients, and 5) further development and validation of the conjugate heat transfer analysis presented here.

Acknowledgments

The authors wish to thank Andreea Dabija, Leo Verling, and Jason McCluskey for their assistance manufacturing, instrumenting, and installing the test piece. The authors would also like to thank Anton Rawlinson and David Bacci for their involvement regarding the blade design and computational modelling, respectively. Finally, the first author would like to express her gratitude to the Holaday Scholarship and the U.S. Air Force for supporting her studies.

References

[1] Han, J.-C., “Advanced Cooling in Gas Turbines 2016 Max Jakob Memorial Award Paper,” *Journal of Heat Transfer*, Vol. 140, No. 13001, 2018. https://doi.org/10.1115/1.4039644.

[2] Coulton, B., “Development of a High Temperature Linear Cascade,” Ph.D. thesis, University of Oxford, 2024. Manuscript in preparation.

[3] Mihailov, S. J., “Fiber Bragg Grating Sensors for Harsh Environments,” *Sensors*, Vol. 12(2), 2012, pp. 1898–1918. https://doi.org/10.3390/s120201898.

[4] Kashyap, R., “Optics and Photonics,” *Fibre Bragg Gratings*, Elsevier, Burlington, MA, 2010, 2^{nd} ed.

[5] Sahota, J., Gupta, N., and Dhawan, D., “Fiber Bragg Grating Sensors for Monitoring of Physical Parameters: A Comprehensive Review,” *Optical Engineering*, Vol. 59(6), No. 060901, 2018. https://doi.org/10.1117/1.oe.59.6.060901.

[6] Bhaskar, C. V. N., Pal, S., and Pattnaik, P. K., “Recent advancements in fiber Bragg gratings based temperature and strain measurement,” *Results in Optics*, Vol. 5, 2021. https://doi.org/10.1016/j.rio.2021.100130.

[7] Xu, M., Archambault, J.-L., Reekie, L., and Dakin, J., “Discrimination between strain and temperature effects using dual-wavelength fibre grating sensors,” *Electronics Letters*, Vol. 30(13), 1994, pp. 1085–1087. https://doi.org/10.1049/el:19940746.

[8] James, S., Dockney, M., and Tatam, R., “Simultaneous independent temperature and strain measurement using in-fibre Bragg grating sensors,” *Electronics Letters*, Vol. 32(12), 1996, pp. 1133–1134. https://doi.org/10.1049/el:19960732.

[9] Ferreira, L., Araujo, F. M., Santos, J. L., and Farahi, F., “Simultaneous measurement of strain and temperature using interferometrically interrogated fiber Bragg grating sensors,” *Optical Engineering*, Vol. 39(8), 2000, pp. 2226–2234. https://doi.org/10.1117/1.1305493.

[10] Willsch, M., Bosselmann, T., Dlohr, P., Kull, R., Ecke, W., Latka, I., Fischer, D., and Thiel, T., “Design of fiber optical high temperature sensors for gas turbine monitoring,” *Proc. SPIE 7503, 20th International Conference on Optical Fibre Sensors*, Vol. 7503, SPIE, 2009. https://doi.org/10.1117/12.835875.

[11] Wang, M., Salter, P., Payne, F., Shipley, A., Morris, S., Booth, M., and Fells, J., “Single-mode sapphire fiber Bragg grating,” *Optics Express*, Vol. 30(9), 2022, pp. 15482–15494. https://doi.org/10.1117/1.1305493.

[12] Xia, H., Byrd, D., Dekate, S., and Lee, B., “High-density fiber optical sensor and instrumentation for gas turbine operation condition monitoring,” *Journal of Sensors*, Vol. 2013, No. 206738, 2013. https://doi.org/10.1155/2013/206738.

[13] Walker, R., Yun, S., Ding, H., Charbonneau, M., Coulas, D., Ramachandran, N., and Mihailov, S., “High-resolution fast temperature mapping of a gas turbine combustor simulator with femtosecond infrared laser written fiber Bragg gratings,” *Proc. SPIE 10110, Photonic Instrumentation Engineering IV*, Vol. 10110, SPIE, San Francisco, 2017. https://doi.org/10.1117/12.2251037.

[14] Murugan, M., Walock, M., Ghosal, A., Knapp, R., and Caesley, R., “Embedded temperature sensor evaluations for turbomachinery component health monitoring,” *Energies*, Vol. 14, 2021. https://doi.org/10.3390/en14040852.

[15] Berexa, E. K., Fells, J. A., and Ireland, P. T., “Viability of Fiber Optic Temperautre Sensors Embedded Withing Engine-Scale Turbine Blades,” *Proceedings of ASME Turbo Expo 2023 Turbomachinery Technical Conference and Exposition - GT2023*, Vol. 4, American Society of Mechanical Engineers, Boston, MA, 2023. https://doi.org/10.1115/GT2023-101440.

[16] Coulton, B., Murray, A. V., and Ireland, P. T., “A Computational Approach to Aerothermal Analysis of Complex Internal Turbine Cooling Geometries,” *Proceedings of ASME Turbo Expo 2022 Turbomachinery Technical Conference and Exposition - GT2022*, Vol. 6-B, American Society of Mechanical Engineers, Rotterdam, The Netherlands, 2022. https://doi.org/10.1115/GT2022-81928.

[17] Kays, W. M., and Crawford, M. E., *Convective Heat and Mass Transfer*, 3^{rd} ed., McGraw-Hill Series in Mechanical Engineering, McGraw-Hill, 1993.

[18] Ngetich, G. C., Murray, A. V., Ireland, P. T., and Romero, E., “A 3D Conjugate Approach for Analysing a Double-Walled Effusion-Cooled Turbine Blade,” *Proceedings of ASME Turbo Expo 2018 Turbomachinery Technical Conference and Exposition - GT2018*, Vol. 2-D, American Society of Mechanical Engineers, Oslo, Norway, 2018. https://doi.org/10.1115/GT2018-76534.

[19] Murray, A. V., Ireland, P. T., and Rawlinson, A. J., "An Integrated Conjugate Computational Approach for Evaluating the Aerothermal and Thermomechanical Performance of Double-Wall Effusion Cooled Systems," *Proceedings of ASME Turbo Expo 2017 Turbomachinery Technical Conference and Exposition - GT2017*, Vol. 5-B, American Society of Mechanical Engineers, Charlotte, North Carolina, 2017. https://doi.org/10.1115/GT2017-64711.

[20] Sellers, J., "Gaseous Film Cooling with Multiple Injection Stations," *AIAA Journal*, Vol. 1:9, 1963, pp. 2154–2156. https://doi.org/10.2514/3.2014.

[21] Ireland, P. T., "Instrument Calibration (Adapted from M. L. G. Oldfield and C. R. Stone)," University of Oxford Lecture Notes, 2006.

[22] Engineering, O., "Types of Thermocouples," https://www.omega.com/en-us/resources/thermocouple-types, 2023.